Article

Journal of the Brazilian Chemical Society

https://dx.doi.org/10.21577/0103-5053.20250012

J. Braz. Chem. Soc. **2025**, *36*, 5, e-20250012, 1-12

Drug Repurposing Strategy to Develop New AZT Derivatives Targeting SARS-CoV-2 Mpro: Synthesis, Computational Studies, and Enzymatic Evaluation

Pedro A. B. Morais,[a] Natália A. Guedes,[a] Caroline S. Fontes,[a] Poliana A. R. Gazolla,[b] Heberth de Paula,[c] Walter C. C. Bigui,[b] Wanderson Romão,[a] Gabriela V. Costa,[d] Adilson V. Costa,[b] Vagner T. de Queiroz,[a,b] and Valdemar Lacerda Júnior[a]*

[a]Programa de Pós-Graduação em Química, Universidade Federal do Espírito Santo, 29075-910 Vitória-ES, Brazil

[b]Grupo de Pesquisa de Estudos Aplicados em Produtos Naturais e Síntese Orgânica (GEAPS-UFES-CNPq), Departamento de Química e Física, Universidade Federal do Espírito Santo, 29500-000 Alegre-ES, Brazil

[c]Departamento de Farmácia e Nutrição, Universidade Federal do Espírito Santo, 29500-000 Alegre-ES, Brazil

[d]Departamento de Química Analítica, Instituto de Química, Universidade Federal do Rio de Janeiro, 21941-598 Rio de Janeiro-RJ, Brazil

This study focused on the synthesis and inhibitory activity of AZT (3'-azido-3'-deoxythymidine) 1,2,3-triazole derivatives against the main protease of severe acute respiratory syndrome coronavirus 2 (SARS-CoV-2), supported by molecular dynamics. The triazoles were synthesized through CuAAC (copper(I)-catalyzed alkyne-azide cycloaddition) with microwave irradiation. Fourier transform infrared spectroscopy (FTIR), ^{1}H and ^{13}C NMR (nuclear magnetic resonance) and mass analyses confirmed the structures of **3a**-**3j**. A luminescence assay was carried out to evaluate main protease (Mpro) inhibition. Molecular dynamics simulation was performed using GROMACS 2023.2. Ten AZT derivatives were synthesized in good yields of 58.7 to 97.7% and NMR data presented correspondent signals for AZT, such as H-8 at 7.76-7.83 and CH_3-9 at 1.77-2.06 as singlets, and H-triazole at 8.03-9.05 as a singlet. Compound **3j** revealed low micromolar inhibitory activity with a half-maximal inhibitory concentration (IC_{50}) value of 25.15 μM. The molecular dynamics simulation showed stable binding interactions over a 200 ns simulation with hydrogen bonds involving Arg188, Gln189, and Gln192 residues, which is similar to nirmatrelvir. The drug repurposing and molecular hybridization approach revealed that AZT is a valid option as a skeleton for new SARS-CoV-2 agents.

Keywords: 3'-azido-3'-deoxythymidine, triazole compounds, SARS-CoV-2 main protease, COVID-19

Introduction

The global COVID-19 (coronavirus disease) pandemic, caused by the SARS-CoV-2 (severe acute respiratory syndrome coronavirus 2) virus, represents one of the most significant global public health crises in history, in addition to directly impacting the global economy.[1] According to data from the World Health Organization (WHO),[2] there has been over 775 million cases of COVID-19 and 7 million confirmed deaths worldwide. Although these numbers continue to rise daily, vaccines are now available to mitigate the symptoms of COVID-19 and reduce the severity of the disease. Currently, 67% of the global population has received at least one dose of the COVID-19 vaccine.[3]

Although vaccines are critical for immunizing the population, studies suggest that careful monitoring of patients on warfarin is also essential. Due to the inflammatory response associated with COVID-19, the efficacy of warfarin may be affected by drug interactions.[4-6] Furthermore, there is evidence that SARS-CoV-2 may influence acetylcholinesterase activity, raising hypotheses regarding the impact of the virus on the nervous system.[7]

*e-mail: pedro.morais@ufes.br; vljuniorqui@gmail.com
Editor handled this article: Brenno A. D. Neto

Thus, antiviral drugs represent an alternative for managing COVID-19 in specific situations.

In addition to vaccines, antiviral drugs are now available to target the proteases involved in the replication of SARS-CoV-2. Among the chymotrypsins encoded by the viral genome, understanding the function and structure of the main protease (Mpro), also known as the 3C-like protease (3CLpro), has been crucial to developing new strategies for controlling COVID-19.[8] Mpro is the enzyme responsible for producing functional viral proteins capable of cleaving polyproteins at specific sites, thereby releasing individual proteins essential for viral replication. Domain I (residues 8-101) and domain II (residues 102-184) of SARS-CoV-2 Mpro resemble an antiparallel β-barrel structure commonly found in serine proteases similar to trypsin, while domain III (residues 201-303) consists of five α-helices. The active site of SARS-CoV-2 Mpro is situated between domains I and II and contains a catalytic dyad composed of histidine and cysteine (His41 and Cys145).[9]

Thus, in addition to the inhibition of the SARS-CoV-2 RdRp (ribonucleic acid (RNA)-dependent RNA polymerase), the inhibition of Mpro has been used as a strategy for the development of drugs aimed at blocking viral replication. Recently, several antiviral drugs targeting Mpro (paxlovid, ensitrelvir, xiannuoxin) and the SARS-CoV-2 RdRp (remdesivir, molnupiravir) have received approval for clinical use. Paxlovid is composed of a Mpro inhibitor (mirmatrelvir) combined with ritonavir, which is an antiretroviral medication commonly used in HIV/AIDS (human immunodeficiency virus/acquired immune deficiency syndrome) treatment in conjunction with other drugs. Xiannuoxin consists of a combination of a Mpro inhibitor (simnotrelvir), ritonavir, and other potential drugs.[10-13] However, the use of these drugs for COVID-19 control presents certain limitations, including low efficacy, poor oral bioavailability, potential toxicity, and suboptimal pharmacokinetic profiles.[14] Nevertheless, due to the emergence of new viral variants resistant to vaccines and currently approved drugs, the search for novel compounds capable of inhibiting viral replication is essential.

Nucleoside analogs and compounds containing a triazole moiety have been investigated for their antiviral activity against SARS-CoV-2.[15,16] Nucleoside analog inhibitors are chemically synthesized derivatives composed of a heterocyclic nucleobase conjugated to either ribose or deoxyribose via a β-glycosidic bond, in which the nucleobase or sugar moiety has been modified.[17] Previous studies[18-24] have evaluated the efficacy of 3'-azido-3'-deoxythymidine (AZT), remdesivir, sofosbuvir, and ribavirin (nucleoside analogs) against SARS-CoV-2 RdRp. The incorporation of these analog compounds into the nucleotide chain prevents the formation of bonds with subsequent nucleotides, thereby blocking the SARS-CoV-2 RdRp reaction.[17] Although several proposals have been published regarding the nucleoside analogs targeting SARS-CoV-2 through RdRp inhibition, information on the effects of nucleoside analogs such as AZT targeting Mpro remains scarce.

Compounds containing a triazole moiety have attracted attention within the scientific community due to their wide range of biological applications. Antiviral activity[25] including inhibition of SARS-CoV-2 replication and viral load reduction in infected cells,[26] leishmanicidal,[27] antimicrobial,[28] antimalarial,[29] antifungal,[30] and anticancer[31] activities, have been reported for this class of bioactive compounds. 1,2,3-Triazole compounds can be synthesized through a click chemistry reaction between a terminal alkyne and an organic azide, catalyzed by copper. This reaction offers significant advantages, including low cost and high yields.[32] Click chemistry is also employed in the formation of molecular hybrids by merging two or more chemical groups, which can enhance their biological activity.[33] The aim of this study was to synthesize and characterize 1,2,3-triazoles derived from AZT (a nucleoside analog) via copper-catalyzed 1,3-dipolar cycloaddition, and evaluate their potential for Mpro inhibition. Additionally, an *in silico* study involving molecular docking and dynamics simulations was conducted to support the enzymatic results.

Experimental

Generalities

Microwave-assisted reactions were performed using the CEM Discover Synthesis Unit (CEM Corp., Matthews, USA), which provides continuous microwave energy with adjustable power up to 300 W. Reactions took place in 10 mL glass vials sealed with septa. Reaction progress was monitored through thin-layer chromatography (TLC) on aluminum plates coated with silica gel F254. Purification was achieved using column chromatography (CC) with silica gel 60 (Merck, Darmstadt, Germany, mesh 70-230) and silica gel 60 ACC (6-35 μm, Chromagel-SDS) as stationary phases, and eluting with mixtures of ethyl acetate, methanol, or hexane. Yields refer to isolated products. Melting points were measured using a Quimis Q-340S13 apparatus. Nuclear magnetic resonance (NMR) spectra were recorded on a Varian 400 MHz spectrometer (Palo Alto, CA, USA) using deuterated dimethyl sulfoxide (DMSO-d_6) and tetramethylsilane (TMS) as internal standards. Chemical shifts (δ) are reported in parts *per* million (ppm) and coupling constants (J) in hertz (Hz). ^{1}H NMR

spectra are annotated with chemical shift δ, multiplicity (s = singlet, d = doublet, t = triplet, m = multiplet), coupling constants (*J* values), and integration. High-resolution mass spectra were obtained with a Bruker Daltonics micrOTOF QII/ESI-TOF (Billerica, USA) through direct injection of the compound dissolved in methanol. This provided an unambiguous molecular formula assignment for singly charged molecular ions, such as $[M + H]^+$ and DBE (double-bound equivalent) values. The infrared (IR) spectrum was recorded on a Bruker Tensor 27 FT-IR spectrometer (Bremen, Germany) scanning from 4000 to 500 cm^{-1}.

Synthetic procedures

Synthesis of 1-(prop-2-yn-1-yl)indoline-2,3-dione (**1**) and 4-allyl-2-methoxy-1-(prop-2-yn-1-yloxy)benzene (**2**)

Compounds **1** and **2** were synthesized and characterized according to the methodologies of Chen *et al.*[34] and Carradori *et al.*[35] respectively. The ^1H and ^{13}C NMR spectra of **1** and **2** were consistent with the reported data.

General procedure for the cycloaddition reactions of azide-alkyne **3a-3j**

Starting from 3'-azido-3'-deoxythymidine (AZT), compounds **3a**-**3j** (Scheme 1) were synthesized via semi-synthesis using both natural and commercial alkynes. The procedure involved combining 0.748 mmol of the alkyne, 0.187 mmol of AZT, 0.018 mmol of sodium ascorbate, and 0.0056 mmol of $CuSO_4.5H_2O$ solution in *N*,*N*-dimethylformamide (DMF) within a sealed 10 mL microwave tube. Microwave irradiation at 150 W and 80 °C for 10 min facilitated the reaction, which was monitored using CCD (central composite design). The resulting product was concentrated using a rotary evaporator and purified through column chromatography on silica.[36]

(1-((1-(2-(Hydroxymethyl)-5-(5-methyl-2,4-dioxo-3,4-dihydropyrimidin-1(2*H*)-yl)tetrahydrofuran-3-yl)-1*H*-1,2,3-triazol-4-yl)methyl)indoline-2,3-dione) (**3a**)

Obtained as yellow solid in 90%; mp 141-158 °C; TLC: retention factor (Rf) = 0.56 (ethyl acetate: methanol 9.5:0.5 v/v); IR (ATR) ν_{max} / cm^{-1} 3263, 1655, 1611, 1272, 1096; ^1H NMR (400 MHz, DMSO-d_6) δ 1.77 (3H, s, CH_3-9), 2.55-2.63 (1H, m, *J* 5.5, 6.7 Hz, Ha-6), 2.63-2.71 (1H, m, *J* 5.9, 6.7 Hz, Hb-6), 3.54-3.59 (1H, m, *J* 3.9, 12.1 Hz, Ha-7), 3.62-3.67 (1H, m, *J* 3.5, 12.1 Hz, Hb-7), 4.13-4.16 (1H, dt, *J* 3.5, 3.9, 8.6 Hz, H-4), 4.96 (2H, s, Ha/Hb-1'), 5.22-5.25 (1H, m, H-O-7), 5.27-5.32 (1H, dt, *J* 5.5, 8.6 Hz, H-3), 6.36 (1H, t, *J* 6.7 Hz, 5,6a, *J* 6.7 Hz, 5,6b, H-5), 7.12 (1H, t, $J_{5',4'}$ 7.82 Hz, $J_{5',6'}$ 7.82 Hz, H-5'), 7.19 (1H, d, *J* 7.8 Hz, H-6'), 7.55 (1H, d, *J* 7.8 Hz, H-3'), 7.65 (1H, t, $J_{4',3'}$ 7.82 Hz, $J_{4',5'}$ 7.82 Hz, H-4'), 7.76 (1H, s, H-8), 8.32 (1H, s, H-trz), 11.31 (1H, s, H-N); ^{13}C NMR (100 MHz, DMSO-d_6) δ 12.65 (CH_3-9), 35.40 (C-1'), 37.43 (C-6), 59.81 (C-3), 61.15 (C-7), 84.31 (C-5), 84.81 (C-4), 110.13 (C-9), 111.56 (C-3'), 117.97 (C-7'), 123.73 (C-5'), 123.92 (C-2), 124.97 (C-6'), 136.67 (C-8), 138.64 (C-4'), 142.20 (C-1), 150.53 (C-2'), 150.85 (C-11), 158.27 (C-9'), 164.25 (C-10), 183.53 (C-8'); HRMS $[M + H]^+$ *m/z*, calcd. for $C_{21}H_{20}N_6O_6$: 452.14, found: 453.1517.

(1-(4-(4-((4-Allyl-2-methoxyphenoxy)methyl)-1*H*-1,2,3-triazol-1-yl)-5-(hydroxymethyl)tetrahydrofuran-2-yl)-5-methylpyrimidine-2,4(1*H*,3*H*)-dione) (**3b**)

Obtained as a white solid in 83.6%; mp 180-193 °C; TLC: Rf = 0.56 (ethyl acetate:methanol 9.5:0.5 v/v); IR (ATR) ν_{max} / cm^{-1} 3406, 1668, 1589, 1260, 1096; ^1H NMR (400 MHz, DMSO-d_6) δ 1.80 (3H, s, CH_3-9),

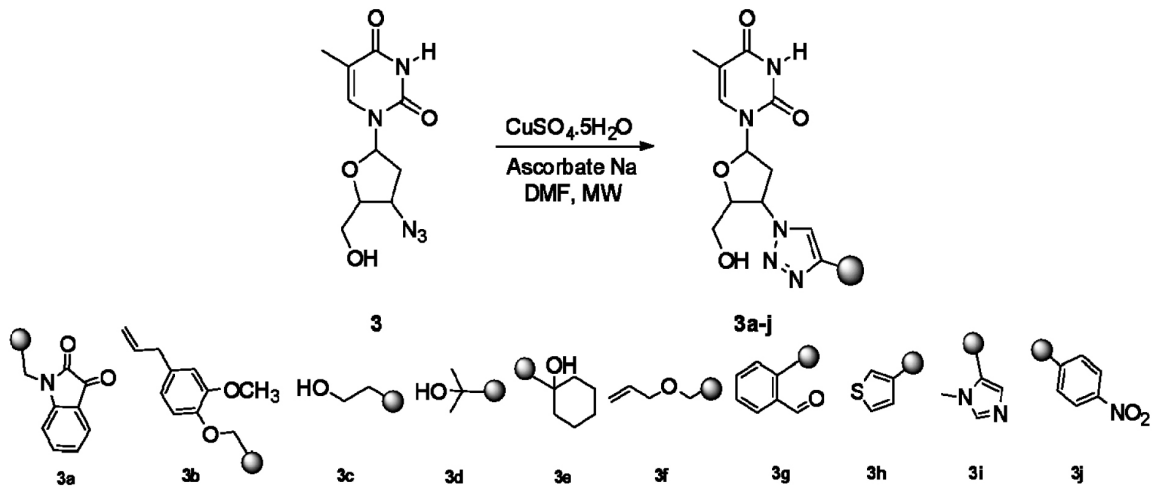

Scheme 1. Formation of compounds **3a**-**3j** via 1,3-dipolar cycloaddition reaction catalyzed by Cu^I from 3'-azido-3'-deoxythymidine (AZT) (**3**).

2.60-2.67 (1H, m, *J* 6.7, 12.5 Hz, Ha-6), 2.69-2.76 (1H, m, *J* 6.7, 12.5 Hz, Hb-6), 3.27-3.29 (2H, d, *J* 6.7 Hz, Ha/Hb-8'), 3.59-3.64 (1H, m, *J* 3.9, 12.1 Hz, Ha-7), 3.67-3.71 (1H, m, *J* 3.5 Hz, Hb-7), 3.71 (3H, s, (H_3C)-O-7'), 4.20-4.23 (1H, dt, *J* 3.5, 3.9, 8.6 Hz, H-4), 4.99-5.01 (1H, dd, *J* 1.2, 10.2 Hz, Ha-10'), 5.02-5.04 (1H, dd, *J* 1.2, 16.8 Hz, Hb-10'), 5.06 (2H, s, Ha/Hb-1'), 5.28-5.30 (1H, m, H-O-7), 5.35-5.40 (1H, dt, *J* 5.5, 8.6 Hz, H-3), 5.88-5.98 (1H, m, *J* 6.7, 10.2, 16.8 Hz, H-9'), 6.41 (1H, t, *J* 6.7 Hz, 5,6a, *J* 6.7 Hz, 5,6b, H-5), 6.67-6.69 (1H, d, *J* 8.2 Hz, H-4'), 6.78 (1H, s, H-6'), 7.02-7.04 (1H, d, *J* 8.2 Hz, H-3'), 7.80 (1H, s, H-8), 8.37 (1H, s, H-trz), 11.34 (1H, s, H-N); ^{13}C NMR (100 MHz, DMSO-d_6) δ 12.66 (CH_3-9), 37.57 (C-6), 39.00 (C-8'), 55.75 (CH_3-O-C-7'), 59.77 (C-3), 61.17 (C-7), 62.13 (C-1'), 84.40 (C-5), 84.88 (C-4), 110.18 (C-9), 112.84 (C-10'), 114.32 (C-6'), 116.05 (C-3'), 120.59 (C-4'), 124.80 (C-2), 133.50 (C-5'), 136.74 (C-8), 138.29 (C-9'), 143.52 (C-1), 146.06 (C-2'), 149. 38 (C-7'), 150.88 (C-11), 164.33 (C-10); HRMS $[M + H]^+$ *m/z*, calcd. for $C_{23}H_{27}N_5O_6$: 469.20, found: 470.2030.

(1-(4-(4-(2-Hydroxyethyl)-1*H*-1,2,3-triazol-1-yl)-5-(hydroxymethyl)tetrahydrofuran-2-yl)-5-methylpyrimidine-2,4(1*H*,3*H*)-dione) (**3c**)

Obtained as a white solid in 83.3%; mp 197-200 °C; TLC: Rf = 0.31 (ethyl acetate:methanol 9.5:0.5 v/v); IR (ATR) ν_{max} / cm^{-1} 1738, 1682, 1373, 1237; ^{1}H NMR (400 MHz, DMSO-d_6) δ 1.79 (3H, s, CH_3-9), 2.57-2.64 (1H, dt, *J* 12.5, 5.5, 6.7 Hz, Ha-6), 2.66-2.72 (1H, m, *J* 12.5, 5.9, 6.7 Hz, Hb-6), 2.76 (2H, t, *J* 7 Hz, Ha-1'/Hb-1', Ha-2', *J* 7 Hz, Ha-1'/Hb-1, Hb-2'), 3.57-3.70 (1H, m, *J* 3.9, 12.1 Hz, Ha-7), 3.57-3.70 (1H, m, *J* 3.5, 12.1 Hz, Hb-7), 3.64 (2H, t, *J* 7 Hz, Ha-2'/Hb-2', Ha-1', *J* 7 Hz, Ha-2'/Hb-2', Hb-1'), 4.16-4.19 (1H, dt, *J* 3.5, 3.9, 8.6 Hz, H-4), 4.68-4.71 (1H, m, H-O-2'), 5.24-5.27 (1H, m, H-O-7), 5.24-5.32 (1H, m, *J* 5.5, 8.6 Hz, H-3), 6.39 (1H, t, *J* 6.7 Hz, 5,6a, *J* 6,7 Hz, 5,6b, H-5), 7.79 (1H, s, H-8), 8.03 (1H, s, H-trz), 11.33 (1H, s, H-N); ^{13}C NMR (100 MHz, DMSO-d_6) δ 12.70 (CH_3-9), 29.51 (C-1'), 37.53 (C-6), 59.46 (C-2'), 60.69 (C-3), 61.21 (C-7), 84.36 (C-5), 84.91 (C-4), 110.14 (C-9), 122.62 (C-2), 136.73 (C-8), 145.19 (C-1), 150.90 (C-11), 164.29 (C-10); HRMS $[M + H]^+$ *m/z*, calcd. for $C_{14}H_{19}N_5O_5$: 337.14, found: 338.1457.

(1-(5-(Hydroxymethyl)-4-(4-(2-hydroxypropan-2-yl)-1*H*-1,2,3-triazol-1-yl)tetrahydrofuran-2-yl)-5-methylpyrimidine-2,4(1*H*,3*H*)-dione) (**3d**)

Obtained as a white solid in 97.6%; mp 165-168 °C; TLC: Rf = 0.24 (ethyl acetate: methanol 9.5:0.5 v/v); IR (ATR) ν_{max} / cm^{-1} 3482, 1687, 1650, 1273, 1090; ^{1}H NMR (400 MHz, DMSO-d_6) δ 1.79 (6H, s, H_3C-1'), 2.06 (3H, s, CH_3-9), 2.57-2.64 (1H, m, *J* 5.5, 6.7 Hz, Ha-6), 2.66-2.73 (1H, m, *J* 5.9, 6.7 Hz, Hb-6), 3.56-3.61 (1H, m, *J* 3.9, 12.1 Hz, Ha-7), 3.65-3.70 (1H, m, *J* 3.5, 12.1 Hz, Hb-7), 4.17-4.20 (1H, dt, *J* 3.5, 3.9, 8.6 Hz, H-4), 5,10 (1H, s, H-O-1'), 5,24-5.26 (1H, m, H-O-7), 5.26-5.33 (1H, dt, *J* 5.5. 5.9 and 8.6 Hz, H-3), 6.39 (1H, t, *J* 6.7 Hz, 5,6a, *J* 6,7 Hz, 5,6b, H-5), 7,79 (1H, s, H-8), 8,06 (1H, s, H-trz), 11,26 (1H, s, H-N); ^{13}C NMR (100 MHz, DMSO-d_6) δ 12.68 (CH_3-9), 31.02 (CH_3-1'), 37.54 (C-6), 59.49 (C-3), 61.21 (C-7), 67.52 (C-1'), 84.33 (C-5), 84.89 (C-4), 110.16 (C-9), 122.67 (C-2), 136.74 (C-8), 150.90 (C-11), 156.45 (C-1), 164.30 (C-10); HRMS $[M + H]^+$ *m/z*, calcd. for $C_{15}H_{21}N_5O_5$: 351.15, found: 352.1611.

(1-(4-(4-(1-Hydroxycyclohexyl)-1*H*-1,2,3-triazol-1-yl)-5-(hydroxymethyl)tetrahydrofuran-2-yl)-5-methylpyrimidine-2,4(1*H*,3*H*)-dione) (**3e**)

Obtained as a white solid in 73.4%; mp 170-174 °C; TLC: Rf = 0.42 (ethyl acetate:methanol 9.5:0.5 v/v); IR (ATR) ν_{max} / cm^{-1} 3387, 1669, 1651, 1263, 1096; ^{1}H NMR (400 MHz, DMSO-d_6) δ 1.21-1.71 (10H, m, H-2', H-3', H-4', H-5', H-6'), 1.79 (3H, s, CH_3-9), 2.57-2.64 (1H, m, *J* 12.5, 5.5 and 6.7 Hz, Ha-6), 2.66-2.73 (1H, m, *J* 12.5, 5.9 and 6.7 Hz, Hb-6), 3.57-3.61 (1H, m, *J* 12.1 Hz, Ha-7), 3.66-3.69 (1H, m, *J* 12.1 Hz, Hb-7), 4.16-4.20 (1H, dt, *J* 3.5, 3.9 and 8.6 Hz, H-4), 4,86 (1H, s, H-O-1'), 5.22-5.27 (1H, m, H-O-7), 5.28-5.33 (1H, dt, *J* 5.5, 5.9, 8.6 Hz, H-3), 6.39 (1H, t, *J* 6.7 Hz, 5,6a, *J* 6.7 Hz, 5,6b, H-5), 7.79 (1H, s, H-8), 8.06 (1H, s, H-trz), 11.12 (1H, s, H-N); ^{13}C NMR (100 MHz, DMSO-d_6) δ 12.66 (CH_3-9), 22.05 (C-4'), 25.59 (C-2',C-6'), 37.50 (C-6), 38.10 (C-3', C-5'), 59.49 (C-3), 61.20 (C-7), 68.47 (C-1'), 84.34 (C-5), 84.90 (C-4), 110.15 (C-9), 121.14 (C-2), 136.73 (C-8), 150.83 (C-11), 156.37 (C-1), 164.30 (C-10); HRMS $[M + H]^+$ *m/z*, calcd. for $C_{18}H_{25}N_5O_5$: 391.19, found: 392.1924.

(1-(4-(4-((Allyloxy)methyl)-1*H*-1,2,3-triazol-1-yl)-5-(hydroxymethyl)tetrahydrofuran-2-yl)-5-methylpyrimidine-2,4(1*H*,3*H*)-dione) (**3f**)

Obtained as a white solid in 58.7%; mp 106-109 °C; TLC: Rf = 0.41 (ethyl acetate:methanol 9.5:0.5 v/v); IR (ATR) ν_{max} / cm^{-1} 3415, 1690, 1659, 1264, 1098; ^{1}H NMR (400 MHz, DMSO-d_6) δ 1.79 (3H, s, CH_3-9), 2.59-2.66 (1H, m, *J* 5.5, 6.7 and 12.5 Hz, Ha-6), 2.69-2.75 (1H, m, *J* 5.9, 6.7 and 12.5 Hz, Hb-6), 3.58-3.63 (1H, m, *J* 12.1 Hz, Ha-7), 3.66-3.71 (1H, m, *J* 3.5, 12.1 Hz, Hb-7), 3.99-4.00 (2H, d, *J* 5.5 Hz, Ha/Hb-2'), 4.18-4.21 (1H, dt, *J* 3.5, 3.9 and 8.6 Hz, H-4), 4.51 (2H, s, Ha/Hb-1'), 5.14-5.17 (1H, dd, *J* 10.6, 1.2 Hz,

Ha-4'), 5.24-5.29 (2H, m, *J* 16.0, 1.2 Hz, Hb-4'/H-O-7), 5.32-5.37 (1H, dt, *J* 5.5, 8.6 Hz, H-3), 5.84-5.93 (1H, m, *J* 5.5, 10.6, 16.0 Hz, H-3'), 6.40 (1H, t, *J* 6.7 Hz, 5,6a, *J* 6.7 Hz, 5,6b, H-5), 7.80 (1H, s, H-8), 8.28 (1H, s, H-trz), 11.33 (1H, s, H-N); ^{13}C NMR (100 MHz, DMSO-d_6) δ 12.67 (CH_3-9), 37.55 (C-6), 59.63 (C-3), 61.16 (C-7), 63.05 (C-1'), 70.75 (C-2'), 84.34 (C-5), 84.87 (C-4), 110.12 (C-9), 117.22 (C-4'), 124.05 (C-2), 135.25 (C-3'), 136.71 (C-8), 144.62 (C-1), 150.87 (C-11), 164.25 (C-10); HRMS $[M + H]^+$ *m/z*, calcd. for $C_{16}H_{21}N_5O_5$: 363.15, found: 364.1609.

(2-(1-(2-(Hydroxymethyl)-5-(5-methyl-2,4-dioxo-3,4-dihydropyrimidin-1(2*H*)-yl)tetrahydrofuran-3-yl)-1*H*-1,2,3-triazol-4-yl) benzaldehyde) (**3g**)

Obtained as a white solid in 97.7%; mp 150-170 °C; TLC: Rf = 0.39 (ethyl acetate:hexane 10:0,1 v/v); IR (ATR) ν_{max} / cm^{-1} 2963, 1741, 1237, 1044; ^{1}H NMR (400 MHz, DMSO-d_6) δ 1.81 (3H, s, CH_3-9), 2.67-2.74 (1H, m, *J* 5.5, 6.7, 12.5 Hz, Ha-6), 2.81-2.87 (1H, m, *J* 5.9, 6.7, 12.5 Hz, Hb-6), 3.66-3.69 (1H, m, *J* 12.1 Hz, Ha-7), 3.72-3.75 (1H, m, *J* 12.1 Hz, Hb-7), 4.30-4.33 (1H, dt, *J* 3.5, 3.9, 8.6 Hz, H-4), 5.27-5.32 (1H, m, H-O-7), 5.42-5.47 (1H, dt, *J* 5.5, 8.6 Hz, H-3), 6.46 (1H, t, *J* 6.7 Hz, 5,6a, *J* 6.7 Hz, 5,6b, H-5), 7.55-7.59 (1H, m, *J* 5.9, 7.8 Hz, H-4'), 7.74-7.78 (2H, m, *J* 5.9 Hz, H2'/H-3'), 7.83 (1H, s, H-8), 7.89 (1H, d, *J* 7.8 Hz, H-5'), 8.84 (1H, s, H-trz), 10.34 (1H, s, H-7'), 11.35 (1H, s, H-N); ^{13}C NMR (100 MHz, DMSO-d_6) δ 12.67 (CH_3-9), 37.53 (C-6), 60.10 (C-3), 61.22 (C-7), 84.45 (C-5), 84.86 (C-4), 110.21 (C-9), 124.74 (C-2), 128.01 (C-1'), 129.12 (C-4'), 130.13 (C-5'), 133.23 (C-2'), 133.76 (C-3'), 134.50 (C-6'), 136.76 (C-8), 144.39 (C-1), 150.90 (C-11), 164.33 (C-10), 193.05 (C-7'); HRMS $[M + H]^+$ *m/z*, calcd. for $C_{19}H_{19}N_5O_5$: 397.14, found: 398.1452.

(1-(5-(Hydroxymethyl)-4-(4-(thiophen-3-yl)-1*H*-1,2,3-triazol-1-yl)tetrahydrofuran-2-yl)-5-methylpyrimidine-2,4(1*H*,3*H*)-dione) (**3h**)

Obtained as a white solid in 74.3%; mp 208-222 °C; TLC: Rf = 0.24 (ethyl acetate:methanol 9.5:0.5 v/v); IR (ATR) ν_{max} / cm^{-1} 3410, 1686, 1663, 1260, 1090; ^{1}H NMR (400 MHz, DMSO-d_6) δ 1.80 (3H, s, CH_3-9), 2.64-2.71 (1H, m, *J* 6.7, 12.5 Hz, Ha-6), 2.74-2.81 (1H, m, *J* 5.9, 6.7, 12.5 Hz, Hb-6), 3.62-3.67 (1H, m, *J* 12.1 Hz, Ha-7), 3.69-3.74 (1H, m, *J* 3.5, 12.1 Hz, Hb-7), 4.24-4.27 (1H, dt, *J* 3.5, 3.9, 8.6 Hz, H-4), 5.28-5.31 (1H, m, H-O-7), 5.35-5.40 (1H, dt, *J* 5.5, 8.6 Hz, H-3), 6.42 (1H, t, *J* 6.7 Hz, 5,6a, *J* 6.7 Hz, 5,6b, H-5), 7.49-7.51 (1H, d, *J* 5.1 Hz, H-2'), 7.63-7.66 (1H, m, *J* 5.1 Hz, H-3'), 7.82 (1H, s, H-8), 7.84-7.85 (1H, d, *J* 2.8 Hz, H-4'), 8.62 (1H, s, H-trz), 11.35 (1H, s, H-N); ^{13}C NMR (100 MHz, DMSO-d_6) δ 12.68 (CH_3-9), 37.53 (C-6), 59.79 (C-3), 61.18 (C-7), 84.36 (C-5), 84.84 (C-4), 110.16 (C-9), 121.19 (C-4'), 121.51 (C-2), 126.16 (C-3'), 127.72 (C-2'), 132.14 (C-1'), 136.73 (C-8), 143.55 (C-1), 150.89 (C-11), 164.28 (C-10); HRMS $[M + H]^+$ *m/z*, calcd. for $C_{16}H_{17}N_5O_4S$: 375.10, found: 376.1068.

(1-(5-(Hydroxymethyl)-4-(4-(1-methyl-1*H*-imidazol-5-yl)-1*H*-1,2,3-triazol-1-yl)tetrahydrofuran-2-yl)-5-methylpyrimidine-2,4(1*H*,3*H*)-dione) (**3i**)

Obtained as a white solid in 72.3%; TLC: Rf = 0.32 (ethyl acetate:methanol 9.5:0.5 v/v); IR (ATR) ν_{max} / cm^{-1} 3379, 1645; ^{1}H NMR (400 MHz, DMSO-d_6) δ 1.80 (3H, s, CH_3-9), 2.63-2.71 (1H, m, *J* 5.5 Hz, Ha-6), 2.75-2.82 (1H, m, *J* 5.9, 6.7, 12.5 Hz, Hb-6), 3.62-3.67 (1H, m, *J* 3.9, 12.1 Hz, Ha-7), 3.69-3.73 (1H, m, *J* 3.5, 12.1 Hz, Hb-7), 3.80 (1H, s, H_3C-N), 4.24-4.28 (1H, dt, *J* 3.5, 8.6 Hz, H-4), 5.29-5.32 (1H, m, H-O-7), 5.38-5.43 (1H, dt, *J* 5.5, 5.9 and 8.6 Hz, H-3), 6.43 (1H, t, *J* 6.7 Hz, 5,6a, *J* 6.7 Hz, 5,6b, H-5), 7.20 (1H, s, H-3'), 7.70 (1H, s, H-2'), 7.82 (1H, s, H-8), 8.61 (1H, s, H-trz), 11.33 (1H, s, H-N); ^{13}C NMR (100 MHz, DMSO-d_6) δ 12.68 (CH_3-9), 33.33 (CH_3-N), 37.54 (C-6), 59.86 (C-3), 61.18 (C-7), 84.37 (C-5), 84.82 (C-4), 110.13 (C-9), 121.95 (C-1'), 123.75 (C-2), 128.22 (C-2'), 136.71 (C-8), 138.08 (C-3'), 140.16 (C-1), 150.89 (C-11), 164.23 (C-10); HRMS $[M + H]^+$ *m/z*, calcd. for $C_{16}H_{19}N_7O_4$: 373.15, found: 374.1563.

(1-(5-(Hydroxymethyl)-4-(4-(4-nitrophenyl)-1*H*-1,2,3-triazol-1-yl)tetrahydrofuran-2-yl)-5-methylpyrimidine-2,4(1*H*,3*H*)-dione) (**3j**)

Obtained as a white solid in 75.1%; mp 232-240 °C; TLC: retention factor (Rf) = 0.33 (ethyl acetate:methanol 9.5:0.5 v/v); IR (ATR) ν_{max} / cm^{-1} 1265, 1226; ^{1}H NMR (400 MHz, DMSO-d_6) δ 1.80 (3H, s, CH_3-9), 2.66-2.74 (1H, m, *J* 6.7, 12.5 Hz, Ha-6), 2.77-2.84 (1H, m, *J* 6.7 Hz, Hb-6), 3.64-3.68 (1H, m, *J* 3.9, 12.1 Hz, Ha-7), 3.68-3.71 (1H, m, *J* 3.5, 12.1 Hz, Hb-7), 4.26-4.29 (1H, dt, *J* 3.5, 3.9, 8.6 Hz, H-4), 5.42-5.47 (2H, m, J 8.6 Hz, H-O-7/H-3), 6.44 (1H, t, *J* 6.7 Hz, 5,6a, *J* 6.7 Hz, 5,6b, H-5), 7.83 (1H, s, H-8), 8.11-8.13 (2H, d, *J* 8.9 Hz, H-2'/H-6'), 8.32-8.34 (2H, d, *J* 8.9 Hz, H-3'/H-5'), 9.05 (1H, s, H-trz), 11.33 (1H, s, H-N); ^{13}C NMR (100 MHz, DMSO-d_6) δ 12.65 (CH_3-9), 37.53 (C-6), 60.21 (C-3), 61.21 (C-7), 84.46 (C-5), 84.84 (C-4), 110.22 (C-9), 123.59 (C-2), 124.87 (C-2', C-6'), 126.48 (C-1'), 136.74 (C-8), 137.27 (C-3', C-5'), 145.09 (C-1), 147.16 (C-4'), 150.90 (C-11), 164.33 (C-10); HRMS $[M + H]^+$ *m/z*, calcd. for $C_{18}H_{18}N_6O_6$: 414.13, found: 415.1176.

Enzymatic assay

Mpro, the 3CL protease of SARS-CoV-2 (final concentration of 16 μg mL^{-1}), was added to a well containing AC-TSTKLQ-aLuc (final concentration of 40 μM) and varying concentrations of inhibitor (1 mM, 1 μM, and 1 nM) in a reaction buffer (4-(2-hydroxyethyl)-1-piperazine ethanesulfonic acid (HEPES) 50 mM, 1,1,1-trichloro2,2-bis(4-chlorophenyl)ethane (DTT) and ethylenediamine tetraacetic acid (EDTA) 0.1 mM, pH 7.2) with a final volume of 25 μL. After a 1-h incubation at 37 °C, 50 μL of detection mixture (Luciferin Detection Reagent and reconstitution buffer, both from Promega) was added. Luminescence was recorded for 30 min at room temperature using a GloMax®-Multi (Promega). The half-maximal inhibitory concentration (IC_{50}) values were determined using luminescence readings at 25 min, plotted as a function of inhibitor concentration with the MLA Quest GraphTM IC_{50} Calculator.[37]

Molecular docking

A docking study using Genetic Optimisation for Ligand Docking (GOLD) 2021.2.0[38] investigated interactions between synthesized compounds and SARS-CoV-2 Mpro (Protein Data Bank (PDB) ID 7M8M; resolution = 1.78 Å). Redocking analyses were performed to determine optimal configurations by evaluating scoring functions and cavity diameters at the binding site. The configurations with the lowest root mean square deviation (RMSD) between the redocking pose and the crystallographic ligand were used for docking the synthesized compounds. The best poses of each compound were analyzed and their key interactions with the protein were highlighted using Proteins Plus web server and PyMOL2.[39]

Molecular dynamics

Molecular dynamics simulations were conducted using GROMACS 2023.2,[40] focusing on the main protease (Mpro) of SARS-CoV-2 in complexes with inhibitors selected from a prior molecular docking step. The initial structures were obtained from the selected docking poses and parameterized using the CHARMM36 force field (July 2022 version).[41] The complexes were placed in a dodecahedral simulation box with a minimum distance of 1.0 nm from the box edges and solvated using the TIP3P water model modified for the CHARMM36 force field. Sodium and chloride ions were added to neutralize the system and achieve a final concentration of 0.15 M.

Energy minimization was performed using the steepest descent algorithm until the maximum force was less than 100.0 kJ mol^{-1} or a maximum of 50,000 steps was reached. Equilibration was conducted in two phases, a 100 ps NVT (constant number of particles, volume, and temperature) phase using the V-rescale thermostat to maintain the temperature at 300 K, followed by a NPT (constant particles pressure and temperature) phase to adjust the pressure to 1 bar using the C-rescale barostat. The production run consisted of a 200 ns simulation with a 2 fs time step, maintaining constant temperature and pressure at 300 K and 1 bar, respectively.

RMSD and RMSF (root mean square fluctuation) analyses were performed using GROMACS tools[40] to assess the stability and local fluctuations of the protein throughout the simulation. The binding free energy (ΔG) was calculated using the PBSA (Poisson-Boltzmann surface area) method implemented in gmx_MMPBSA v1.6.3,[42] with sampling from the trajectory starting at frame 100 with an interval of 100 frames, at a temperature of 298.15 K, and considering standard solvent and volume parameters. Additionally, an interaction map was generated using in house Python scripts, employing the pandas, matplotlib, and seaborn libraries, along with the PLIP tool.[43] PLIP was used to extract molecular interaction data from the simulations, such as hydrogen bonds and salt bridges. These data were then compiled into a single DataFrame using pandas and visualized through scatter plots where different types of interactions were distinctly colored using Matplotlib and seaborn.

Results and Discussion

Chemistry

The CuAAC click reactions synthesized AZT derivatives with yields ranging from 58.7 to 97.7%. The structure of the compounds was confirmed through spectroscopic techniques (NMR and IR) and spectrometric techniques (HRMS, high-resolution mass spectra). The strong carbonyl stretching band in the IR spectra of compounds **3a**-**3j** (Scheme 1) was observed in the range of 1682-1655 cm^{-1}, and the O–H stretching band was centered between 3482-3264 cm^{-1}. The presence of the carbonyl group between the nitrogen atoms in the pyrimidine ring of AZT derivatives was confirmed through signals observed in the ^{13}C NMR spectra at 150.8-150.90 ppm. The carbonyl carbon adjacent to the methyl group appears at 164.23-164.33 ppm, while the neighboring methyl carbon is observed at 12.65-12.70 ppm. The carbon C-5 of the pentose linked to the pyrimidine ring shows a signal at

84.31-84.46 ppm, and the carbon C-4 attached to the hydroxymethyl group appears at 61.15-61.22 ppm. The carbon in the triazole ring is detected at 120.67-124.80 ppm, and its adjacent carbon bound to alkynes shows a signal at 140.16-156.45 ppm. The hydrogen in the triazole ring was observed as a singlet in the ^{1}H NMR spectra in the range of 8.03-9.05 ppm. In the pyrimidine ring, the methyl group appear as a singlet at 1.77-2.06 ppm, the hydrogen bonded to the nitrogen between the carbonyl groups appears at 11.22-11.35 ppm, and the hydrogen adjacent to the nitrogen attached to the pentose appears at 7.76-7.88 ppm, all as singlets. The molecular mass of the AZT derivatives was verified through HRMS analyses. The analysis data showed a strong correlation with the structures of the synthesized compounds. The spectra used for the characterization of the compounds are available in the Supplementary Information (SI) section (Figures S1-S50).

Biological evaluation

Subsequently, the ten novel AZT derivatives were submitted to enzymatic inhibitory activity, which was carried out following a previously published procedure,[37] using the substrate AC-TSTKLQ-aLuc (final concentration of 40 μM). A mixture of enzyme and substrate, in the absence of inhibitors, was applied as a negative control. Two compounds, **3a** and **3j**, showed moderate to good inhibitory activity against SARS-CoV-2 3CLpro with IC_{50} values of 89.18 and 25.15 μM, respectively.

As previously mentioned, Mpro plays a crucial role in viral replication by cleaving the viral polyprotein into functional proteins necessary for generating new viruses. Several studies[24,44] have highlighted the significance of Mpro as a valid target for the development of new antiviral drugs against SARS-CoV-2.

Kumar *et al.*[45] evaluated 26 isatin-based compounds against SARS-CoV-2 Mpro, revealing IC_{50} values ranging from 0.65 to 5.5 μM. Similarly, ElNaggar *et al.*[46] synthesized six new sulphonamide-tethered *N*-((triazol-4-yl)methyl)isatin derivatives, with IC_{50} values ranging from 0.25 to 17 μM. Docking simulations interestingly highlighted that the most active compound performs a similar binding mechanism with the co-crystallized ligand, interacting with Ser144, His41, Met 165, and Cys145 residues through H-bond, and one hydrophobic interaction with Glu166.

Recent research highlights the nitro group present in compound **3j** as a potential pharmacophore for the development of new antiviral drugs against SARS-CoV-2. Another recent study[47] investigated the antiviral activity of nitro compounds derived from quinazoline against the SARS-CoV-2 Mpro enzyme and found promising inhibitory activity.

Molecular docking study

To predict the binding mode of the most active inhibitor, **3j** docking parameters were selected based on the lowest RMSD values. Table 1 shows the scoring function and cavity size values at the binding site around the crystallographic ligand. The best parameters did not consider water or flexible residues at the binding site. For the remaining docking simulations, the criteria used on the software for the SARS-CoV-2 Mpro (PDB ID 7M8M; resolution = 1.78 Å) were: (*i*) the binding site within 10 Å (around the crystallographic ligand), and (*ii*) the ChemPLP scoring function, which was used to rank the generated conformations. All other settings were kept as default.

Table 1. Scoring functions and diameters used in the redocking study. The table presents the redocking efficiency in terms of RMSD

Diameter / Å	Scoring function			
	ChemPLP	GoldScore	ChemScore	ASP
5	0.926	0.606	0.997	0.949
7	0.549	0.750	0.582	0.438
10	0.412	0.424	0.946	0.421

RMSD: root mean square deviation; ChemPLP: piecewise linear potential; ASP: astex statistical potential.

The molecular docking results between compound **3j** and SARS-CoV-2 Mpro revealed several interactions that may contribute to the stability of the formed complex. Firstly, hydrogen bonds involving the ligand and specific residues of the active site of the protein were observed. The hydrogen from the amino group and one of the oxygen atoms of the pyrimidine ring of the ligand form hydrogen bonds with Gln192, with distances of 2.2 and 2.1 Å, respectively; the triazole ring forms a hydrogen bond with Glu166 (2.1 Å); and the oxygen of the nitro group establishes a hydrogen bond with Gly143 (2.2 Å). In addition to hydrogen bonds, significant π-alkyl interactions were also identified. The pyrimidine ring interacts with Pro168 (3.2 Å) and the pentose with Met165 (2.9 Å). The π-sulfur interactions can also be observed between the pyrimidine ring and Met165 (5.9 Å) and the nitrobenzyl ring and Cys145 (3.3 Å) (Figure 1).

Molecular dynamics study

The overall conformational stability of the Mpro protein complexes were evaluated using molecular

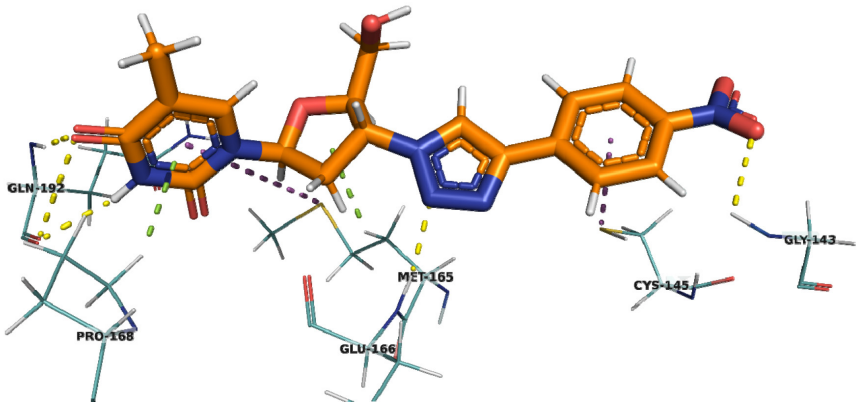

Figure 1. Binding mode and molecular interactions of **3j** with the SARS-CoV-2 Mpro active site. Hydrogen bonds are represented by yellow dashed lines; π-alkyl interactions are represented by green dashed lines; π-sulfur interactions are represented by magenta dashed lines; the involved amino acid residues are represented by blue lines.

dynamic simulations in its apo form and when bound to two distinct ligands, the novel compound **3j** and the established antiviral drug nirmatrelvir. The simulations revealed that the apo form of the Mpro protein maintained an average RMSD of 0.25 nm (Figure 2), indicating a high degree of structural stability. Upon binding with **3j** and nirmatrelvir, the average RMSD values decreased slightly to 0.24 nm for both complexes (Figure 2). This suggests that the presence of these ligands did not induce significant structural disturbances in the protein, allowing it to maintain its conformational integrity over the 200 ns simulation period. The similar RMSD values observed for both ligands indicate that **3j**, despite being a novel compound, stabilizes the protein structure as effectively as nirmatrelvir.

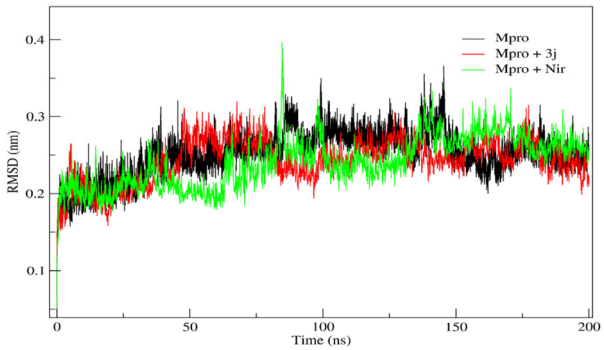

Figure 2. The RMSD graph of SARS-CoV-2 Mpro (black), the **3j** (red) and nirmatrelvir (green) complexes.

RMSF was used to assess the mobility of individual residues within the protein over time. The RMSF analysis revealed that in the apo form, certain regions of Mpro, particularly between residues His41 and Met49, exhibited greater flexibility (Figure 3).

However, the binding of nirmatrelvir significantly reduced the fluctuation in this region, which can be attributed to halogen interactions between the fluorine atoms of nirmatrelvir and His41, Cys44, and Thr45 residues (Figures 3b and 4a).

This reduction in mobility indicates a stabilization effect, which is further corroborated by the lower RMSF values. In contrast, the **3j**-bound complex displayed a higher degree of fluctuation in this region compared to the nirmatrelvir complex, albeit less than the apo form. The increased flexibility observed in the Mpro + **3j** complex could be due to fewer halogen interactions, which leads to a less pronounced stabilization effect. However, in the region between Asp187 and Gln192 residues (Figure 3c), both ligand-bound complexes demonstrated reduced fluctuation compared to the apo form, with **3j** exhibiting slightly higher fluctuations, potentially due to more transient hydrogen bond interactions.

A detailed examination of the molecular interactions during the 200 ns simulations revealed critical insights into the binding mechanisms of nirmatrelvir and **3j**. The temporal interaction map (Figure 4a) of the Mpro + nirmatrelvir complex identified several persistent interactions, including halogen, hydrogen bonds, and pi-stacking interactions. These interactions, particularly the hydrogen bonds with Ser46, Met49, Tyr54, Glu166, Asp187, Arg188, and Gln189 residues, were consistently observed throughout the simulation.

Halogen interactions were notably frequent with Thr25, Thr26, His41, Cys44, Thr45, Gly143, Cys145, and His164 residues. These interactions likely contribute to the observed stability of the complex, particularly the recurring interactions with Thr25 and Cys44 during the first 100 ns, which later shifted to Gly143 and Cys145. Pi-stacking interactions were also observed, albeit less frequently, particularly with His41.

For the Mpro + **3j** complex, hydrogen bonds were the predominant interaction type, involving Arg188, Gln189,

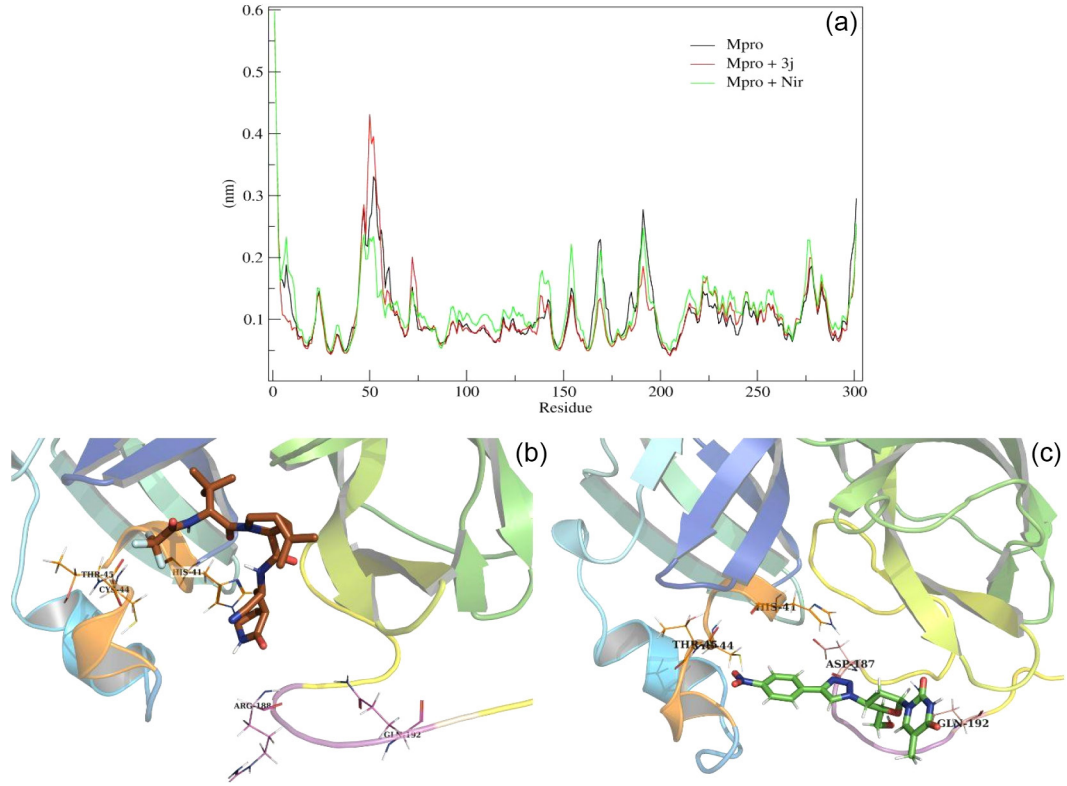

Figure 3. (a) The RMSF graph of SARS-CoV-2 Mpro (black) and the **3j** (red) and nirmatrelvir (green) complexes. 3D interactions performed by (b) nirmatrelvir and (c) **3j** within the active site of the Mpro.

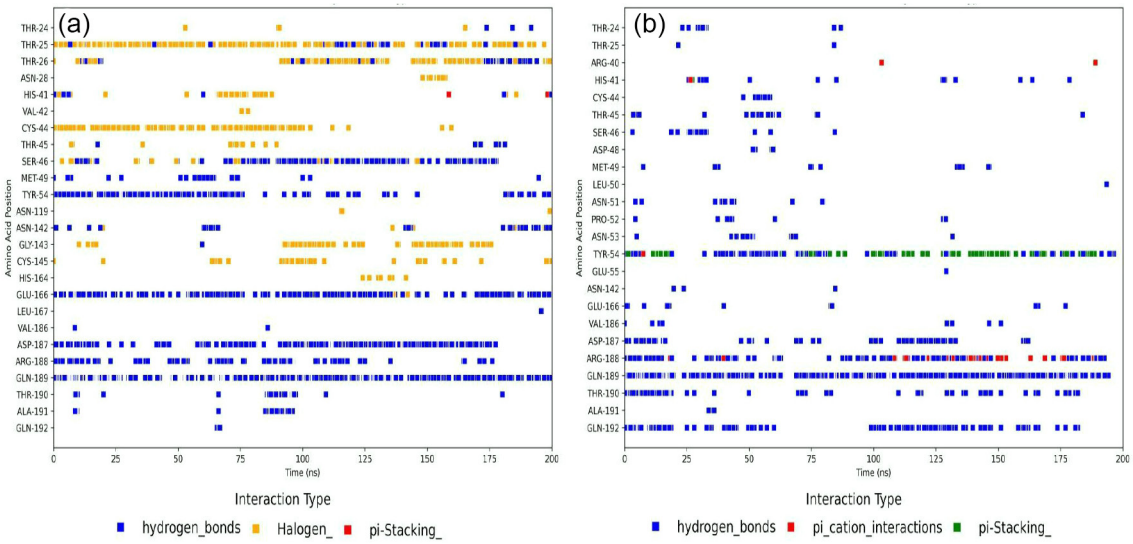

Figure 4. Temporal interaction map of Mpro + nirmatrelvir (a) and Mpro + **3j** (b) complexes.

and Gln192 residues (Figure 4b). Although less common, Pi-cation interactions were also identified, particularly with Arg40, His41, and most frequently with Arg188. Continuous π-stacking interactions were observed with Tyr54, suggesting that the aromatic ring of **3j** may engage in stabilizing interactions throughout the simulation.

The ΔG for both complexes was calculated using the PBSA method to provide quantitative insights into the binding affinity of the ligands. The ΔG values obtained were –21.41 ± 0.54 kJ mol^{-1} for the Mpro + **3j** complex and –22.83 ± 0.70 kJ mol^{-1} for the Mpro + nirmatrelvir complex. These results indicate that both ligands exhibit strong binding affinities to the Mpro protein, with nirmatrelvir demonstrating slightly more favorable binding energy. The relatively close ΔG values suggest that the novel compound **3j** has a binding affinity comparable to

that of nirmatrelvir, which is consistent with the stability observed in the RMSD and RMSF analyses. The slightly more negative ΔG for nirmatrelvir may be attributed to the additional halogen interactions, which may enhance overall binding stability. In contrast, the diverse interaction profile of **3j**, including pi-cation and pi-stacking interactions, may provide alternative stabilization mechanisms, potentially making it a promising candidate for further therapeutic development.

In the ADMET (absorption, distribution, metabolism, excretion, and toxicology) analysis of compounds **3j** and Nir, the results revealed that both compounds exhibited similar pharmacological and pharmacodynamic properties within the tested biological system (Table 2).

Despite the potential differences in chemical structure or intended therapeutic use, the two compounds demonstrated comparable profiles across the key ADMET parameters. This lack of significant differences suggests that both **3j** and Nir exhibit similar behaviors in terms of how they are absorbed, distributed throughout the body, metabolized, and excreted. Additionally, their toxicity profiles are also aligned, indicating that neither compound presents a markedly higher risk of adverse effects compared to the other under the tested conditions. This information is valuable for further drug development and optimization, as it indicates that both compounds could be considered equally viable candidates based on their ADMET profiles.

Conclusions

Considering the social and economic impact of the COVID-19 pandemic caused by the SARS-CoV-2 virus, and the emergence of several variants such as EBA.2.86, JN.1 and KP.2, the successful repurposing strategy with remdesivir opened the doors to explore drugs as building blocks to create new chemical weapons targeting the main protease of SARS-CoV-2. AZT, which is a nucleoside analogue like remdesivir, was applied as a skeleton for the synthesis of ten novel triazole derivatives through CuAAC, using a hyphenated technique of microwave reactor discovery, in a good yield. The coupling of heterocycles and natural products with well-established biological properties was carried out using a molecular hybridization strategy. As a result, AZT derivative **3j** revealed good micromolar inhibitory activity, 25.15 μM, against SARS-CoV-2 Mpro, supported by a robust computational study related to molecular dynamic simulations that presented stability and H-bond interactions similar to nirmatrelvir. As such, it is also worth addressing drug repurposing and molecular hybridization strategies to synthesize potential new anti-SARS-CoV-2 agents to expand the chemical weapons against new virus variants.

Supplementary Information

Supplementary information (IR, NMR, and high-resolution mass spectra) is available free of charge at http://jbcs.sbq.org.br as PDF file.

Table 2. The ADMET results of ligands **3j** and Nir in pharmacokinetic and pharmacodynamic properties

Property	Model name	Complex property	
		Mpro + Nir	Mpro + **3j**
Absorption	HIA / %	0.931	0.993
	Caco-2 cell / (nm s^{-1})	–5.360	–5.550
	MDCK	–5.080	–4.360
Distribution	skin permeability	–1.500	–0.690
	BBB	–2.230	–3.360
Metabolism	CYP-2C19-inhibition	non-inhibitor	non-inhibitor
	CYP-2C9-inhibition	non-inhibitor	non-inhibitor
	CYP-2D6-inhibition	non-inhibitor	non-inhibitor
	CYP-2D6-substrate	non-substrate	non-substrate
	CYP-3A4-inhibition	non-inhibitor	non-inhibitor
	CYP-3A4-substrate	substrate	non-substrate
	mutagenicity (Ames test)	toxic	toxic
	carcinogenicity rat	none	none
	HERG inhibition	toxic	toxic

ADMET: absorption, distribution, metabolism, excretion, and toxicology; HIA: human intestinal absorption; MDCK: madin darby canine kidney; BBB: blood-brain barrier; HERG inhibition: human ether-a-go-go related gene inhibition; Nir: nirmatrelvir; Mpro: main protease.

Acknowledgments

This study was financed in part by Coordenação de Aperfeiçoamento de Pessoal de Nível Superior (CAPES, Brazil - finance code 001), Fundação de Amparo à Pesquisa e Inovação do Espírito Santo (FAPES, Brazil - public notice 11/2019, term of grant 532/2020; public notice 03/2020, term of grant 313/2020; public notice 003/2021, term of grant 472/2021; public notice 021/2022, term of grant 1055/2022) and Conselho Nacional de Desenvolvimento Científico e Tecnológico (CNPq, Brazil, grant No. 306873/2021-4). The authors are supported by research fellowships from FAPES (V. T. Q.) and CNPq (A. V. C., W. R., and V. L. J.). The authors would like to thank the researchers from the graduate program in Agrochemistry (UFES), Group of Organic and Medicinal Chemistry in Alegre (GAQUOM/UFES/CNPq), and Natural Products and Organic Synthesis Research Group (GEAPS/UFES/CNPq) for their learning support.

Author Contributions

Pedro A. B. Morais was responsible for funding acquisition, project administration, supervision, writing (review and editing); Natália A. Guedes for investigation, validation, visualization, writing original draft; Caroline S. Fontes for investigation, validation, visualization, writing original draft; Poliana A. R. Gazolla for investigation, validation, visualization, writing original draft; Heberth de Paula for funding acquisition, project administration, supervision, writing (review and editing); Walter C. C. Bigui for investigation, validation, visualization, writing original draft; Wanderson Romão for data curation, formal analysis; Gabriela V. Costa for data curation, formal analysis; Adilson V. Costa for funding acquisition, project administration, supervision, writing (review and editing), Vagner T. de Queiroz for funding acquisition, project administration, supervision, writing (review and editing); Valdemar Lacerda Júnior for funding acquisition, project administration, supervision, writing (review and editing).

References

1. Biernacki, K.; Ciupak, O.; Daśko, M.; Rachon, J.; Flis, D.; Budka, J.; Inkielewicz-Stępniak, I.; Czaja, A.; Rak, J.; Demkowicz, S.; *J. Enzyme Inhib. Med. Chem.* **2024**, *39*, 2290910. [Crossref]
2. World Health Organization (WHO), *Number of COVID-19 Cases Reposted to WHO*, https://data.who.int/dashboards/covid19/cases?n=c, accessed in December 2024.
3. World Health Organization (WHO), *COVID-19 Vaccination*, https://data.who.int/dashboards/covid19/vaccines, accessed in December 2024.
4. The OpenSAFELY Collaborative; Wong, A. Y. S.; Tomlinson, L. A.; Brown, J. P.; Elson, W.; Walker, A. J.; Schultze, A.; Morton, C. E.; Evans, D.; Inglesby, P.; MacKenna, B.; Bhaskaran, K.; Rentsch, C. T.; Powell, E.; Williamson, E.; Croker, R.; Bacon, S.; Hulme, W.; Bates, C.; Curtis, H. J.; Mehrkar, A.; Cockburn, J.; McDonald, H. I.; Mathur, R.; Wing, K.; Forbes, H.; Eggo, R. M.; Evans, S. J. W.; Smeeth, L.; Goldacre, B.; Douglas, I. J.; *J. Hematol. Oncol.* **2021**, *14*, 172. [Crossref]
5. Comissão Nacional de Incorporação de Tecnologias no Sistema Único de Saúde (CONITEC); *Diretrizes Brasileiras para Tratamento Hospitalar do Paciente com COVID-19*; Ministério da Saúde: Brasília, 2021, ch. 2. [Link] accessed in December 2024
6. Li, H.; Wang, Y.; Fan, R.; Lv, H.; Sun, H.; Xie, H.; Tang, T.; Luo, J.; Xia, Z.; *Drug Des., Dev. Ther.* **2016**, *10*, 2173. [Crossref]
7. Charlie-Silva, I.; Araújo, A. P. C.; Guimarães, A. T. B.; Veras, F. P.; Braz, H. L. B.; Pontes, L. G.; Jorge, R. J. B.; Belo, M. A. A.; Fernandes, B. H. V.; Nóbrega, R. H.; Galdino, G.; Condino-Neto, A.; Galindo-Villegas, J.; Machado-Santelli, G. M.; Sanches, P. R. S.; Rezende, R. M.; Cilli, E. M.; Malafaia, G.; *J. Hazard. Mater.* **2021**, *419*, 126463. [Crossref]
8. Zagórska, A.; Czopek, A.; Fryc, M.; Jończyk, J.; *Biomolecules* **2024**, *14*, 797. [Crossref]
9. Wang, W. W.; Zeng, P.; Liu, T.; Zhou, X. L.; Lin, C.; Guo, L.; Wang, Q. S.; Li, J.; *J. Mol. Biol.* **2024**, *436*, 168784. [Crossref]
10. Hu, S.; Jiang, S.; Qi, X.; Bai, R.; Ye, X. Y.; Xie, T.; *Drug Dev. Res.* **2022**, *83*, 16. [Crossref]
11. US Food and Drug Administration (FDA), *Coronavirus (COVID-19) Update: FDA Issues Emergency Use Authorization for Potential COVID-19 Treatment*, https://www.fda.gov/news-events/press-announcements/coronavirus-covid-19-update-fda-issues-emergency-use-authorization-potential-covid-19-treatment, accessed in December 2024.
12. Rahmah, L.; Abarikwu, S. O.; Arero, A. G.; Essouma, M.; Jibril, A. T.; Fal, A.; Flisiak, R.; Makuku, R.; Marquez, L.; Mohamed, K.; *Pharmacol. Rep.* **2022**, *74*, 1255. [Crossref]
13. US Food and Drug Administration (FDA), *FDA Approves First Oral Antiviral for Treatment of COVID-19 in Adults*, https://www.fda.gov/news-events/press-announcements/fda-approves-first-oral-antiviral-treatment-covid-19-adults, accessed in December 2024.
14. Huang, C.; Shuai, H.; Qiao, J.; Hou, Y.; Zeng, R.; Xia, A.; Xie, L.; Fang, Z.; Li, Y.; Yoon, C.; Huang, Q.; Hu, B.; You, J.; Quan, B.; Zhao, X.; Guo, N.; Zhang, S.; Ma, R.; Zhang, J.; Wang, Y.; Yang, R.; Zhang, S.; Nan, J.; Xu, H.; Wang, F.; Lei, J.; Chu, H.; Yang, S.; *Signal Transduction Targeted Ther.* **2023**, *8*, 128. [Crossref]
15. Holanda, V. N.; Lima, E. M. A.; da Silva, W. V.; Maia, R. T.; Medeiros, R. L.; Ghosh, A.; Lima, V. L. M.; de Figueiredo, R. C. B. Q.; *J. Biomol. Struct. Dyn.* **2022**, *40*, 5462. [Crossref]
16. Abdalla, M.; Rabie, A. M.; *Comput. Biol. Chem.* **2023**, *104*, 107768. [Crossref]

17. Daikopoulou, V.; Apostolou, P.; Mourati, S.; Vlachou, I.; Gouguosi, M.; Papasotiriou, I.; *Molecules* **2021**, *26*, 3461. [Crossref]
18. Chien, M.; Anderson, T. K.; Jockusch, S.; Tao, C.; Li, X.; Kumar, S.; Russo, J. J.; Kirchdoerfer, R. N.; Ju, J.; *J. Proteome Res.* **2020**, *19*, 4690. [Crossref]
19. Frediansyah, A.; Nainu, F.; Dhama, K.; Mudatsir, M.; Harapan, H.; *Clin. Epidemiol. Global Health* **2021**, *9*, 123. [Crossref]
20. Jácome, R.; Campillo-Balderas, J. A.; de León, S. P.; Becerra, A.; Lazcano, A.; *Sci. Rep.* **2020**, *10*, 9294. [Crossref]
21. Khalili, J. S.; Zhu, H.; Mak, N. S. A.; Yan, Y.; Zhu, Y.; *J. Med. Virol.* **2020**, *92*, 740. [Crossref]
22. Reina, J.; *Rev. Esp. Quimioter.* **2020**, *33*, 176. [Crossref]
23. Tong, S.; Su, Y.; Yu, Y.; Wu, C.; Chen, J.; Wang, S.; Jiang, J.; *Int. J. Antimicrob. Agents* **2020**, *56*, 106114. [Crossref]
24. Wang, M.; Cao, R.; Zhang, L.; Yang, X.; Liu, J.; Xu, M.; Shi, Z.; Hu, Z.; Zhong, W.; Xiao, G.; *Cell Res.* **2020**, *30*, 269. [Crossref]
25. Rodrigues, J. V. S.; Gazolla, P. A. R.; Pereira, I. C.; Dias, R. S.; da Silva, I. E. P.; Prates, J. W. O.; Gomes, I. S.; Silveira, S. A.; Costa, A. V.; de Oliveira, F. M.; de Aguiar, A. R.; da Silva, C. C.; Teixeira, R. R.; de Paula, S. O.; *Antiviral Res.* **2023**, *212*, 105578. [Crossref]
26. Ng, J. P. L.; Yun, Y. X.; Nasim, A. A.; Gianoncelli, A.; Law, B. Y. K.; Ribaudo, G.; Wong, V. K. W.; Coghi, P.; *Bioorg. Chem.* **2023**, *141*, 106882. [Crossref]
27. Gazolla, P. A. R.; Lima, W. P.; de Aguiar, A. R.; Borsodi, M. P. G.; Costa, A. V.; de Oliveira, F. M.; de Oliveira, O. V.; Costa, M. C. A.; Ferreira, M. M. C.; do Nascimento, C. J.; Junker, J.; Vaz, B. G.; Teixeira, R. R.; *Future Med. Chem.* **2024**, *16*, 139. [Crossref]
28. Kumar, V.; Lal, K.; Kumar, R.; Kumar, A.; Mathpati, R. S.; Singh, M. B.; Kumari, K.; *Future Med. Chem.* **2023**, *15*, 1115. [Crossref]
29. Batra, N.; Agarwal, D.; Ishan, U.; Tekuri, C. S.; Gupta, R. D.; Nath, M.; *Future Med. Chem.* **2022**, *14*, 1725. [Crossref]
30. Lima, A. M. A.; Moreira, L. C.; Gazolla, P. R.; Oliveira, M. B.; Teixeira, R. R.; Queiroz, V. T.; Rocha, M. R.; Moraes, W. B.; dos Santos, N. A.; Romão, W.; Lacerda Jr., V.; Morais, P. A. B.; de Oliveira, O. V.; Jesus Jr., W. C.; Barbosa, L. C. A.; Nascimento, C. J.; Junker, J.; Costa, A. V.; *J. Agric. Food Chem.* **2024**, *72*, 12459. [Crossref]
31. Oubella, A.; Alossaimi, M. A.; Riadi, Y.; Bhat, M. A.; Bakheit, A. H.; Taha, M. L.; Auhmani, A.; Morjani, H.; Geesi, M. H.; Itto, M. Y. A.; *Future Med. Chem.* **2024**, *16*, 1449. [Crossref]
32. Martinho, L. A.; Andrade, C. K. Z.; *Tetrahedron* **2024**, *157*, 133964. [Crossref]
33. Ouyang, T.; Liu, X.; Ouyang, H.; Ren, L.; *Virus Res.* **2018**, *256*, 21. [Crossref]
34. Chen, G.; Wang, Y.; Hao, X.; Mu, S.; Sun, Q.; *Chem. Cent. J.* **2011**, *5*, 37. [Crossref]
35. Carradori, S.; Ammazzalorso, A.; Niccolai, S.; Tanini, D.; D'Agostino, I.; Melfi, F.; Capperucci, A.; Grande, R.; Sisto, F.; *Pharmaceuticals* **2023**, *16*, 1317. [Crossref]
36. Jawalekar, A. M.; Meeuwenoord, N.; Cremers, J. S. G. O.; Overkleeft, H. S.; van der Marel, G. A.; Rutjes, F. P. J. T.; van Delft, F. L.; *J. Org. Chem.* **2008**, *73*, 287. [Crossref]
37. Sondag, D.; Merx, J.; Rossing, E.; Boltje, T. J.; Löwik, D. W. P. M.; Nelissen, F. H. T.; van Geffen, M.; van't Veer, C.; van Heerde, W. L.; Rutjes, F. P. J. T.; *ChemBioChem* **2022**, *23*, e202200190. [Crossref]
38. Jones, G.; Willett, P.; Glen, R. C.; Leach, A. R.; Taylor, R.; *J. Mol. Biol.* **1997**, *267*, 727. [Crossref]
39. *PyMOL Molecular Graphics System*, version 3.0.5; Schrödinger, LLC, USA, 2002.
40. Abraham, M. J.; Murtola, T.; Schulz, R.; Páll, S.; Smith, J. C.; Hess, B.; Lindahl, E.; *SoftwareX* **2015**, *1-2*, 19. [Crossref]
41. Huang, J.; Rauscher, S.; Nawrocki, G.; Ran, T.; Feig, M.; de Groot, B. L.; Grubmüller, H.; MacKerell Jr., A. D.; *Nat. Methods* **2017**, *14*, 71. [Crossref]
42. Valdés-Tresanco, M. S.; Valdés-Tresanco, M. E.; Valiente, P. A.; Moreno, E.; *J. Chem. Theory Comput.* **2021**, *17*, 6281. [Crossref]
43. Adasme, M. F.; Linnemann, K. L.; Bolz, S. N.; Kaiser, F.; Salentin, S. Haupt, V. J.; Schroeder, M.; *Nucleic Acids Res.* **2021**, *49*, 530. [Crossref]
44. Jin, Y.; Yang, H.; Ji, W.; Wu, W.; Chen, S.; Zhang, W.; Duan, G.; *Viruses* **2020**, *12*, 372. [Crossref]
45. Kumar, R.; Gideon, D. A.; Mariadasse, R.; Nirusimhan, V.; Castin, J.; Jeyakanthan, J.; Dhayabaran, V. V.; *J. Biomol. Struct. Dyn.* **2022**, *40*, 6710. [Crossref]
46. ElNaggar, M. H.; Elgazar, A. A.; Gamal, G.; Hamed, S. M.; Elsayed, Z. M.; El-Ashrey, M. K.; Abood, A.; El Hassab, M. A.; Soliman, A. M.; El-Domany, R. A.; *J. Enzyme Inhib. Med. Chem.* **2023**, *38*, 2234665. [Crossref]
47. Zhou, S.; Wang, K.; Hu, Z.; Chen, T.; Dong, Y.; Gao, R.; Wu, M.; Li, Y.; Ji, X.; *Eur. J. Med. Chem.* **2023**, *261*, 115831. [Crossref]

Submitted: October 16, 2024
Published online: January 22, 2025